Ore Geology Reviews 104 (2019) 589–602

Contents lists available at ScienceDirect

Ore Geology Reviews

journal homepage: www.elsevier.com/locate/oregeorev

Invited Review Article

Applications of synchrotron X-ray techniques to orogenic gold studies; examples from the Timmins gold camp

Jessica M. Stromberg[a,*], Lisa L. Van Loon[a], Robert Gordon[b,c], Arthur Woll[d], Renfei Feng[e], Dirk Schumann[f], Neil R. Banerjee[a]

[a] Department of Earth Sciences, Western University, 1151 Richmond st., London, ON N6A 5B7, Canada
[b] Department of Physics, Simon Fraser University, 8888 University Drive Burnaby, British Columbia V5A 1S6, Canada
[c] PNC–CAT, Sector 20, Advanced Photon Source, Building 401, Argonne National Laboratory, 9700 Cass Ave, Lemont, IL 60439, USA
[d] Cornell High Energy Synchrotron Source, Cornell University, 161 Wilson Laboratory, Synchrotron Dr., Ithaca, NY 14853, USA
[e] Canadian Light Source, 44 Innovation Blvd., Saskatoon, Saskatchewan S7N 2V3, Canada
[f] Fibics Incorporated, 1431 Merivale Rd #100, Ottawa, Ontario K2E 0B9, Canada

ARTICLE INFO

Keywords:
Synchrotron
X-ray fluorescence
Trace element geochemistry
Orogenic gold
Metal speciation
Pyrite

ABSTRACT

Understanding the association between precious metals and trace elements in ore minerals is integral to ore deposit research and exploration. *In situ* characterization of ore minerals is now at the forefront of this field. The power of *in situ* element mapping and characterization is the ability to combine geochemistry with mineralogical and broader geological context. Synchrotron radiation (SR) X-ray techniques such as X-ray Fluorescence (XRF) and X-ray Absorption Near Edge Spectroscopy (XANES) are incredibly powerful tools for studying ore systems with applications in exploration, geometallurgy, and remediation. We provide examples of these applications to gold-bearing samples from across the world-class Timmins gold camp in Canada. Analysis of thin sections, billet offcuts, as well as cut rock slabs highlights the versatility of SR-XRF and XANES analysis at multiple stages of deposit investigation and for multiple sample types. SR-XRF mapping of large areas at 20 μm resolution is very effective for quickly identifying and characterizing gold and trace element associations with gold, even in low grade and nuggety samples. Large area mapping is integral to quickly providing key geochemical information within the sample context as well as for improving efficiency and mitigating bias in grain selection for higher resolution analyses. High-resolution SR-XRF mapping and XANES analysis of individual mineral grains are compared to conventional EPMA mapping and reveals micrometer scale associations with trace metals, Au, and As. The characterization of trace element associations with different fluid events and gold mineralization styles is integral to understanding mineralizing systems and developing exploration vectors. Point XRF and XANES identified and characterized the presence and nature of refractory gold in pyrite as well as grain scale variability in As speciation. An early understanding of the distribution and redox state of gold, trace metals, and deleterious elements at the exploration stage has implications for mitigating future geometallurgy and remediation issues. The examples presented highlight the potential for the application of synchrotron studies early in the mine cycle for characterizing gold mineralization in orogenic systems.

1. Introduction

The use of synchrotron X-ray techniques is well established in the field of environmental science research (see Fenton, 2002 for a review), as well as in the remediation and environmental research sectors of the mining industry (e.g., Manceau et al., 2002; Sutton et al., 2002; Walker et al., 2005; Fawcett and Jamieson, 2011; Etschmann et al., 2014; Wang et al., 2016; Blanchard et al., 2017). However, applications for ore deposit studies, exploration and production (geometallurgy) are underdeveloped. With advances in x-ray fluorescence detector technologies and x-ray optics, the main limiting factors for the application of this advanced technique (low availability, perceived high cost, long collection times) are mitigated, and applications to ore deposit characterization are being explored (e.g., Fisher et al., 2015; Li et al., 2016; Etschmann et al., 2017; Pearce et al., 2017; Barnes et al., 2017a,b). However, the integration of multiple synchrotron radiation microanalysis tools to orogenic gold deposits has not previously been described. This study presents examples of synchrotron radiation

* Corresponding author at: CSIRO Mineral Resources, Perth, WA 6151, Australia.
E-mail address: jessica.stromberg@csiro.au (J.M. Stromberg).

https://doi.org/10.1016/j.oregeorev.2018.11.015
Received 12 March 2018; Received in revised form 9 November 2018; Accepted 17 November 2018
Available online 20 November 2018
0169-1368/

Table 1
Sample Information. Au, As, and Ag values are in ppm.

Sample #	Mine	Host	Type	Sample	Au	Ag	As
C406932	Dome	Vipond Formation	Ankerite Vein	Thin Section	0.9	< 0.5	177
C406934	Dome	Vipond Formation	Ankerite Vein	Thin Section	5.7	4.7	90
E885276	Hoyle Pond	Porcupine Assemblage	Greywacke	Thin Section (Qtz)	4.68		
C408781	Dome	Gold Center Formation	Interflow Sediment	Thin Section (Qtz)	98.1	16.4	> 10,000
C408779	Dome	Timiskaming Conglomerate	Sulfide Clast	Thin Section and Slab	2.73	22.5	486
C410901	N/A	Vipond Formation	Ankerite Vein	Slab	0.36	< 0.5	87
B-A	Buffalo-Ankerite	Hersey Lake Formation	Ankerite Vein	Slab	0.5	< 0.5	45

techniques applied to the characterization of gold, pyrite and trace metals in a variety of depositional settings in the world class Timmins gold camp in Canada. (See Table 1).

1.1. Pyrite geochemistry

There is a large body of work on the characterization of trace elements and gold in pyrite due its ubiquity in many ore deposit types (e.g., Deditius et al., 2008; Large et al., 2014; Tardani et al., 2017; Muhkerjee and Large, 2017). Pyrite can incorporate metals as solid solution and nanoparticles under a wide range of conditions, preserving valuable information about the chemical evolution of the fluid from which it precipitates (e.g., Palenik et al., 2004; Large et al., 2009; Cook et al., 2013; Reich et al., 2005; Deditius et al., 2014). This makes pyrite trace element content a powerful tool for understanding the geochemistry of depositional environments, and for enhancing exploration and ore processing.

The relationship between Au and As in pyrite has been studied in detail, primarily in the context of Carlin type deposits, and is integral for effective ore processing and remediation as the nature refractory gold (nanoparticle vs lattice bound) impacts the extraction process (e.g., Cook and Chryssoulis, 1990; Simon et al., 1999; Cabri et al., 2000; Reich et al., 2005; Deditius et al., 2008, 2011, 2014; Sykora et al., 2018). The nature of refractory gold in pyrite is well characterized, and occurs as both metallic Au^0 nanoparticles, and Au^{1+} in the crystal lattice of the pyrite (e.g., Cabri et al., 2000; Reich et al., 2005). The As content and speciation (As^{1-} vs. As^{3+}) in arsenian pyrite can play a role in the distribution of refractory gold mineralization and the introduction of other commonly deleterious trace elements into pyrite as As^{3+} has been related to greater uptake of trace metals (Reich et al., 2005; Deditius et al., 2008). Understanding associations of other trace elements (e.g., Cu, Ni, Co, W) with gold in pyrite has implications for improving exploration in regions with complex mineralization histories by identifying and characterizing distinct fluid events and for early detection of potential remediation issues related to the release of deleterious elements (e.g., Feick 2016; Muhkerjee and Large, 2017; Sykora et al., 2018). There are multiple techniques that are commonly employed for *in situ* analysis of mineral grains applied to ore deposits, with electron probe microanalysis (EPMA), secondary ion mass spectrometry (SIMS), and laser ablation inductively coupled plasma mass spectrometry (LA-ICP-MS) being the most common. For each of these techniques there are trade-offs between image resolution, mappable area, limits of detection, and the number of elements detected (Fig. 1; see Pearce et al., 2017 for a review).

1.2. In situ geochemistry

The foundation for the effective application of high-resolution ore mineral characterization and larger scale interpretations of ore forming processes is robust characterization of sample context given the complexity and heterogeneity of geologic samples (e.g., Schumann et al., 2014). This is traditionally done by petrographic methods such as optical microscopy and backscatter scanning electron microscopy (BSE-SEM) (e.g., Large et al., 2009; Sykora et al., 2018). More recently, some

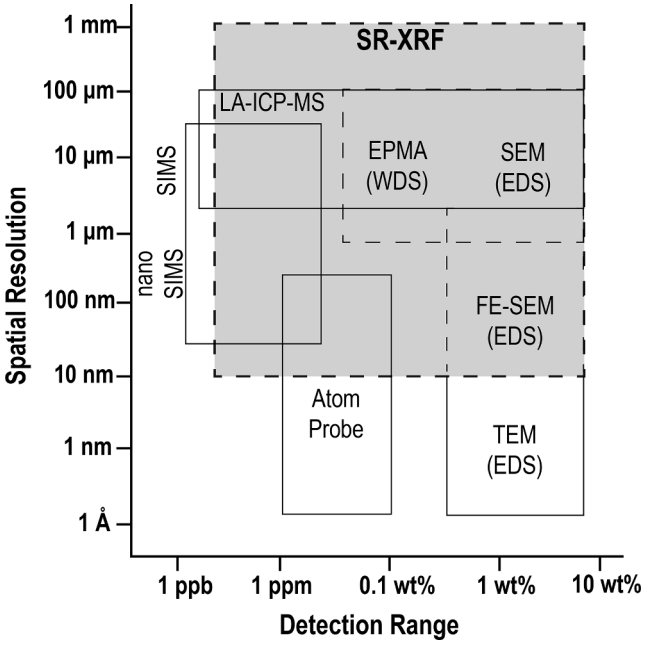

Fig. 1. Comparison of the spatial resolution and detection range of micro-analytical trace element mapping techniques. LA-ICP-MS: laser-ablation inductively-coupled plasma mass spectrometry; SR-XRF: synchrotron X-ray fluorescence; EPMA: electron probe micro-analysis; WDS: wavelength dispersive X-ray spectrometry; SEM: scanning electron microscopy; EDS: energy dispersive X-ray spectrometry; (nano) SIMS: secondary ion mass spectrometry; FE-SEM: field emission scanning electron microscopy; TEM: transmission electron microscopy. Techniques with dashed outlines are non-destructive. (modified from Reich et al., 2017).

of these have been automated to characterize entire thin sections and may also include energy-dispersive X-ray spectrometry (EDS), which provides chemical information (e.g., QEMSCAN, Mineralogic Mining, ZEISS Atlas 5.0). The reality in the mining sector is that key questions regarding exploration and processing need to be answered early and on short time frames. The ability to optimize the conventional workflow by bringing high-resolution analysis to the front end while also gaining key contextual information represents a paradigm shift (e.g., Ryan et al., 2018a,b).

LA-ICP-MS has become the technique of choice for *in situ* quantitative trace element analysis with high spatial resolution in ore deposit studies (e.g., Large et al., 2009; 2011, 2014, 2017; Muhkerjee and Large, 2017). This technique can measure both major and trace elements with 5–50 µm (typically 15–50 µm) spatial resolution, but is destructive to the sample (Pearce et al., 2017). Historically, the standard tool in metallurgy is mineral liberation analysis (MLA), which is based on a scanning electron microscope (SEM) platform (Jones, 1987; Petruk, 2000; Pearce et al., 2017). Electron probe micro-analysis (EPMA) also utilizes a SEM platform, but with a wavelength dispersive spectroscopy (WDS) detection system that allows for better precision in detection of minor elements, as well as elements whose emission lines

are close in energy (e.g., Pt-Lα and Au-Lα), or have multiple line interferences (e.g., the REE). EPMA can in some cases achieve sub-micron mapping resolution, but the area that can be mapped is restricted by time and the number of elements that can be analyzed (Pearce et al., 2017). Secondary ion mass spectrometry (SIMS) is considered the benchmark technique for quantification of submicroscopic gold and is commonly used in gold deportation studies (e.g., Dimov and Hart, 2011). SIMS analysis has lower detection limits than EPMA, however, is destructive to the sample. Samples analyzed by SIMS, EPMA and LA-ICP-MS are generally prepared as thin sections or mounted in epoxy as a polished surface is required.

1.3. Synchrotron X-ray fluorescence (XRF)

Like other X-ray fluorescence (XRF) methods, synchrotron radiation (SR) based micro-XRF is a non-destructive technique. It allows for the *in situ* mapping of major and trace elements on the nanometer to micron scale with minimal sample preparation (Fig. 1). Both polished thin sections and whole rock samples can be analyzed, each with their own set of caveats. Float glass, which is typically used for thin section preparation, contains trace element impurities (e.g., As, Mn (Supplementary materials)) that depending on the density and thickness of the sample material can affect measurements due to the high flux of a synchrotron X-ray source. In addition to reduced sample preparation, the flexibility of synchrotron end stations permit for a variety of sample sizes and shapes to be analyzed under atmospheric conditions. The experimental set-up is customizable and the excitation energy is tunable, making for few limitations in terms of number of elements analyzed. The application of synchrotron SR-XRF mapping to ore deposit studies has traditionally been restricted due to availability and cost of beam time as well as long data acquisition times. However, with advances in detector technology, its application to mapping trace elements in ore minerals has been pursued (e.g., Fisher et al., 2015; Li et al., 2016; Barnes et al., 2017a,b). The introduction of the Maia detector (384 element Si detector) allows for very fast data collection (millisecond dwell times) with high-count rates (millions of counts; Ryan et al., 2010a,b, 2013, 2014). This makes it possible to characterize an entire thin section or rock slab at 20 µm resolution within a few hours. While in house µXRF instruments are now available with comparable spatial resolutions (e.g., Bruker Tornado, Sigray AttoMap™), they are not tunable and cannot achieve the high flux of a synchrotron source and so mapping at the sample scale is not practical, and specific emissions cannot be targeted.

Unlike conventional *in situ* geochemical techniques (EPMA, SIMS, LA-ICP-MS), SR-XRF analysis produces full spectrum data sets that can identify elements present within a complex geologic sample that are excited by the incident energy of the beam with ppm detection limits (Fig. 1). The plethora of minor and trace elements found in pyrite, as well as the inherent difficulty in characterizing trace elements in gold make SR-XRF mapping a very effective technique for exploring the relationship between gold, trace elements and pyrite in orogenic systems. Additionally, the non-destructive nature of SR-XRF analysis makes it very complementary to other techniques, allowing for follow up analysis by destructive nano-scale techniques, such as high-resolution transmission electron microscopy (HR-TEM), nanoSIMS, and atom probe. This includes other synchrotron X-ray techniques, such as XANES (x-ray absorption near edge spectroscopy), which provides information on trace metal speciation (e.g., Cabri et al., 2000; Etschmann et al., 2017).

1.4. X-ray absorption near edge spectroscopy (XANES)

Synchrotron based research in ore deposit studies has primarily focused on XANES analysis to study experimentally controlled systems and processes, or very well constrained samples (see Brugger et al., 2010 for a review). For example, metal complexing in fluid inclusions and experimental fluids (e.g., Brown, 1990; Bancroft and Hyland, 1990; Mavrogenes et al., 2002; Etschmann et al., 2017), speciation of Au and other trace metals in sulfides (e.g., Cabri et al., 2000; Cook et al., 2013), and biogeochemical processes related to gold and platinum nugget formation (e.g., Campbell et al., 2015; Shuster et al., 2015). XANES has also been extensively applied to mining remediation studies to characterize the speciation of metals and metalloids in environmental samples (e.g., Walker et al., 2005; Fawcett and Jamieson, 2011; Blanchard et al., 2017). Advances in detector technology have also had an impact on the application of XANES analysis with the development of XRF stacking for speciation mapping, which has been applied to environmental, uranium ore, and As uptake into apatite (e.g., Etschmann et al., 2014, 2017; Lui et al., 2017). However, this technique has yet to be applied to pyrite-rich gold ore samples. The benchmark tool for investigations of Au and As in pyrite is generally SIMS analysis. However, the methods and workflow by which pyrite-rich ores are traditionally characterized may be improved by the adoption of synchrotron radiation based techniques, such as XANES and SR-XRF.

2. Methods

2.1. Sample preparation

Slabs were cut from whole rock samples and standard polished thin sections were prepared from selected samples. Aliquots of the whole rock samples were sent for bulk rock geochemistry by inductively coupled plasma-atomic-emission spectrometry (ME-ICP06 -Whole Rock Package ICP-AES) and inductively coupled plasma mass spectrometry (ME-MS81 – Lithium Borate Fusion ICP-MS) respectively, following pulverization at ALS Minerals in Sudbury, Canada. Samples were mounted both on standard float glass and quartz slides. The use of quartz slides for thin section preparation mitigates the issue of contamination from glass trace element content. The remaining slabs and blocks from thin section preparation were preserved. Thin sections were characterized by conventional light microscopy and backscattered electron scanning electron microscopy (BSE-SEM). BSE-SEM analysis was undertaken at the Western Nanofabrication facility where samples were coated with 5 nm amorphous osmium and imaged on a LEO (Zeiss) 1540 XB field emission gun – scanning electron microscope (FEG-SEM) that was operated at 10 kV.

2.2. Synchrotron radiation – X-ray fluorescence (SR-XRF) maps

SR-XRF data was collected over multiple visits at three different third generation synchrotron source facilities (Canadian Light Source VESPERS beam line, Cornell High Energy Synchrotron Source F3 beam line, Advanced Photon Source 20-ID). All beam lines used are hard x-ray beam lines with microprobe stations optimized for SR-XRF on different spatial scales. The details of each synchrotron, beam line, and their analytical capabilities are summarized in the Supplementary data.

Thin sections and off-cuts were affixed onto custom designed aluminum sample holders and mounted on the sample translation stage. Samples were raster-scanned through the focused beam to collect full spectrum XRF data for each pixel across regions of interest within the sample. Element maps were collected with an incident X-ray energy of 13.1 keV (APS and CHESS) and with the up to 20 keV pink (polychromatic) beam at the CLS. The spatial resolution ranged from 2 to 20 µm and dwell times ranged from 4 msec to 1 s. All experimental mapping parameters are summarized in the Supplementary data. Standard foils (Au, Mn, Fe, Sb) were used for energy calibration and NIST standard SRM 1834 and implanted SIMS standards were analyzed to determine beamline parameters for post processing.

2.3. X-ray absorption near edge spectroscopy

Individual XANES spectra were collected at the APS on beam line

20-ID to determining the oxidation states of gold and arsenic. The energy position was calibrated to the gold L3 edge (E_0 11,919 eV) using the first peak of the first derivative XANES spectrum of a metallic gold foil standard. Energy scales were referenced to the gold foil spectrum. The scan parameters of the XANES spectra with respect to E_0 were from −150 to −20 eV with 5 eV steps, −20 to 20 eV with 0.5 eV steps, and 20 eV to 9 k with 0.05 k steps. E_0 is defined by the edge of interest (11919 eV for Au L-edge and 11868 eV for the As K-edge). An integration time of 1s was used. Three (3) to five (5) scans were collected for each point depending on the concentration of the element of interest.

XANES mapping was performed at the CHESS F3 beam line by collecting stacked SR-XRF elemental maps using the MAIA detector (Kirkham et al., 2010; Ryan et al., 2010a,b, 2014). Regions for stacked map and point XANES collection were selected from the Au and As XRF maps of entire samples and data was also collected from Au and As standards (arsenopyrite and metallic gold). Experimental parameters were chosen to step over both the As K edge (11867 eV) and the Au L3 edge (11919 eV) with high energy resolution (0.5 eV) and are summarized in the Supplementary data.

2.4. Electron probe Micro-Analysis (EPMA)

Electron probe maps were collected with a JEOL JXA-8530f field emission electron microbe at the Earth and Planetary Materials Analysis Laboratory at the University of Western Ontario. Pyrite maps were collected for the following elements: As, Cu, Zn, Au, Ni with a wavelength dispersive x-ray spectrometer (WDS), and Fe and S with the energy dispersive spectrometer (EDS) at 0.5 and 2 μm beam diameter. Pure metal standards were used for the WDS maps (As-Gallium arsenide, gold, copper, nickle, zinc) to refine peak position for maximum counts, and for the Fe and S EDS maps the default ranges from the EDS detector were used. Maps were collected with an accelerating voltage of 15 kV, 200 nA and a dwell time of 10 ms. Maps were created without any manipulation to show the full spectrum of counts.

3. Data analysis

3.1. Peakaboo

SR-XRF maps collected at the CLS were processed using Peakaboo, a software program developed by the University of Western Ontario as a part of the Science Studio package (McIntyre et al., 2010). Peakaboo allows for the identification of peaks in the XRF spectrum such as K, L, and M fluorescence lines, escape peaks, and pileup peaks. It fits peaks using a Gaussian function with preset widths, and the identification of an element requires a close fit of multiple lines in the spectrum, each with its own shape. Fits also take into account details such as separations and relative intensities of Kα 1 and 2, Kβ 1, 2, and 3, Lα, Lβ 1 and 2, Lγ 1, 2, and 3 lines. The intensity of peaks for selected elements can be plotted as a function of their spatial distribution in the sample creating a spatially resolved elemental map. A 90% Brukner background removal is applied to the mean averaged spectrum for the entire map to suppress background from X-ray scattering, and then the mean average spectrum is fitted. For the fitting of spectral peaks a Gaussian function is used with preset widths, and the identification of an element requires a close fit to multiple lines in the spectrum. Following peak fitting, two-dimensional maps are created to show the distribution of selected element using two interpolation (smoothing) passes.

3.2. 2D-scan Plot

High resolution mapping data from APS ID-20 was analyzed using in house software (2D Q-Scan Plot). 2D Q-Scan Plot processes full spectrum data and simultaneously creates intensity maps for preselected regions of interest (ROI's) within the full spectrum. Up to fifteen regions of interest were preselected based on the expected chemistry of the sample. In general, the peak widths are ~420 eV wide. However, the regions were refined prior to mapping by collecting point spectra from representative regions of the sample and adjusted to minimize the effects of peak overlap.

3.3. Athena

Athena 8.054 (Ravel and Newville, 2005) was used to processes the XANES data. The spectra were normalized to the intensity of the incident beam measured with an ion chamber upstream of these sample. In Athena an energy calibration is performed to the gold L-edge with a gold foil measured under the same experimental conditions. Pre- and postedge processing follows standard methods (e.g., Dyer et al., 2001) where the pre-edge was fit with a linear regression (−100 to −30 eV) relative to edge position), and the post-edge was fit with a second order polynomial for normalization. Sample spectra was compared with reference spectra collected during the experiment as well as reference spectra from the literature.

3.4. GeoPIXE

Large-scale maps collected at CHESS F3 were analyzed using GeoPIXE, a software suite that uses a fundamental parameters approach with spectral deconvolution and imaging using the dynamic analysis (DA) method (Ryan et al., 2010a). This is based on fitting a representative total spectrum and detailed model of the Maia detector array efficiency, the details of which are outlined in Ryan et al. (2010). This method results in a matrix transformation, which can produce real time and offline projections of full spectrum data into elemental maps yielding both qualitative and quantitative data and provide mineral specific trace element contents (e.g., Fisher et al., 2015). For real time mapping we created a bulk rock matrix, which approximates the average composition of auriferous pyrite-rich samples. This was then refined and refit using sample specific information with yields calculated using the specific matrix for that sample or region of interest with the sample.

For the XRF stacks, a list of incident energies was created in GeoPIXE. The SR-XRF spectrum at the highest incident energy was fitted, and a XANES energy series DA matrix was formed. The same DA matrix was used to extract the As images from maps collected at lower incident energies. By extracting the As peak area for each pixel in all the SR-XRF images XANES spectra were formed at each pixel. Quantitative XANES stacking analysis may be achieved by methods such as PCA and linear combination fitting (e.g., Etschmann et al., 2010, 2014). This is particularly important for larger and more heterogeneous datasets. However, at present a qualitative evaluation of our dataset is sufficient to demonstrate the capability of XANES stacking analysis for identifying changes in As redox on the grain scale.

4. Results

4.1. EPMA mapping

Detailed microscopy identified two euhedral pyrite grains in the pyrite-rich vein margin of sample C46932. The grains contain small ~10 μm gold inclusions and BSE-SEM identified an As-rich core (Fig. 2a). Trace element mapping by both EPMA and SR-XRF revealed that the As-rich core of the pyrite is made up of arsenopyrite inclusions as well as arsenian pyrite and identifies the presence of Cu, and Zn-rich inclusions, and zones of Ni enrichment in the pyrite which overprint the As-rich core (Fig. 2b, c). EPMA mapping provided slightly more detail in the As and Ni maps, showing finer structure in the enrichments as the map resolution is 0.5 μm compared to 2 μm for the SR-XRF maps.

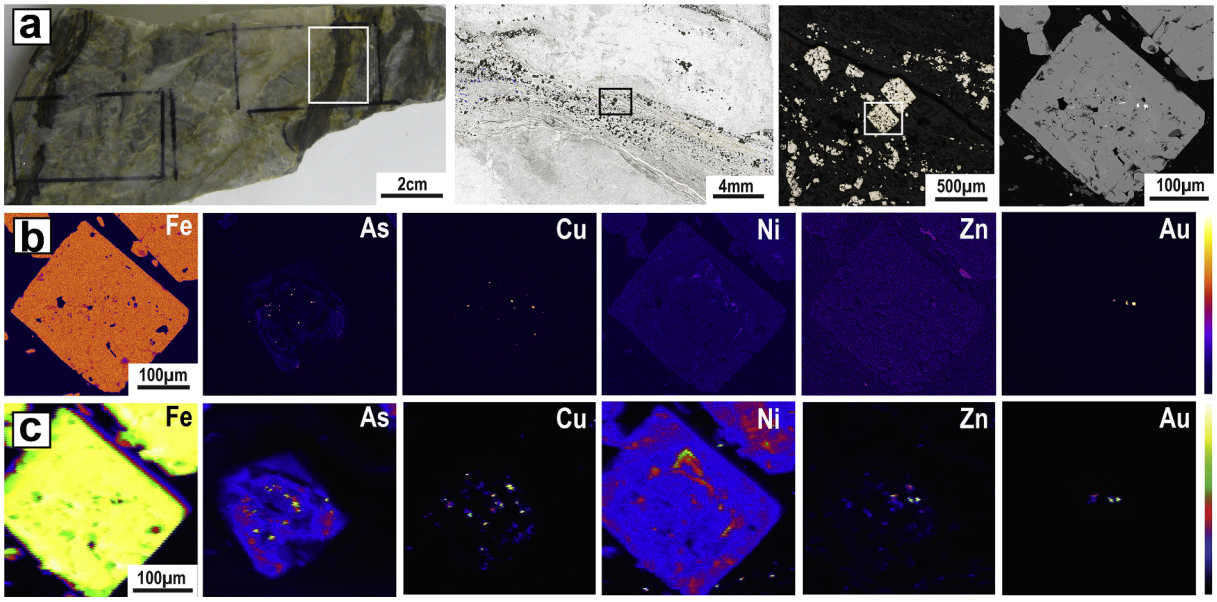

Fig. 2. Comparison of EPMA and SR-XRF mapping of individual pyrite grains using the conventional workflow for high-resolution analysis (C406932). A. Grain selection for high-resolution analysis generally begins with selecting regions of interest from a whole rock sample for thin section preparation, in this case the pyrite-rich vein a thin section followed by characterization by conventional light microscopy and BSE-SEM. B. 0.5 µm resolution EPMA trace element maps of a grain of interest C. 2 µm resolution SR-XRF maps of the same grain show comparable resolution of inclusions and trace element distributions but with full spectrum data collection.

4.2. Multi-scale SR-XRF mapping

4.2.1. Sample E885276

SR-XRF mapping of a sample of auriferous greywacke reveals multiple styles of sulfide mineralization and identifies the relationship between Au and sulfides in the sample (Fig. 3). The sample is a sericite altered greywacke dominated by with quartz and carbonate stringers. Coarse 20 µm resolution mapping (Fig. 3a) reveal that the sample

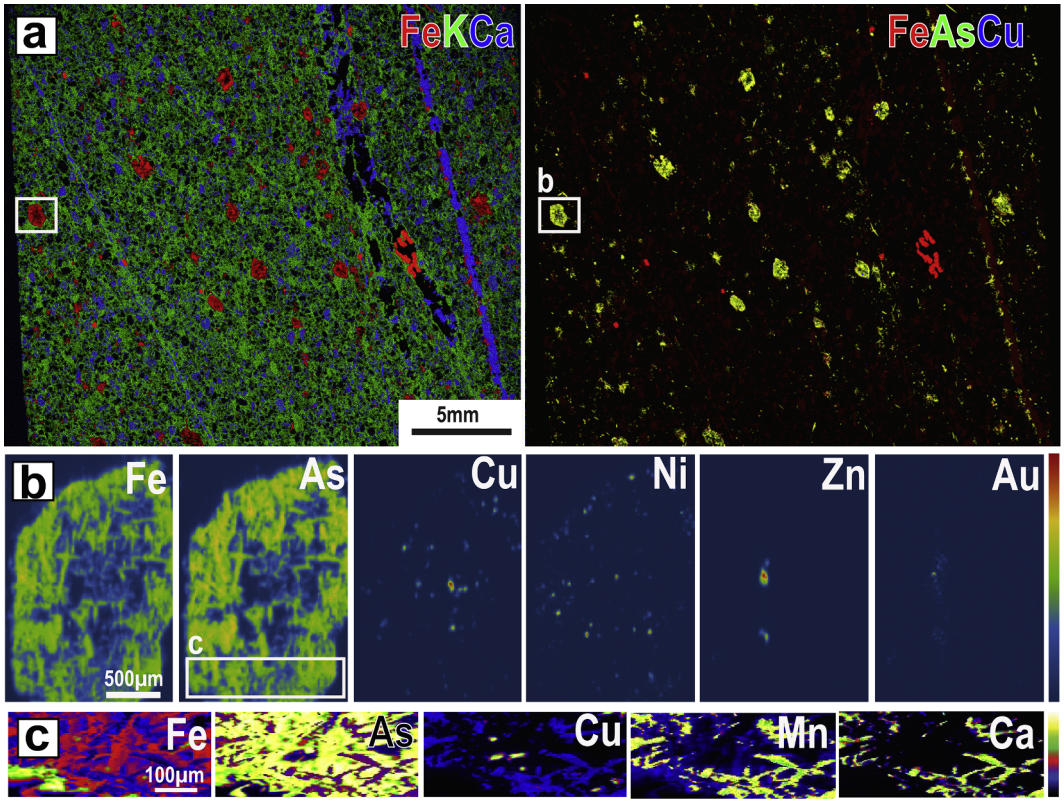

Fig. 3. SR-XRF maps of sample E885276. A. 20 µm resolution RGB maps of a thin section mounted on a quartz slide reveal potassic and carbonate alteration as well as several styles of sulfide mineralization. B. 8 µm resolution mapping shows that Cu and Ni are associated with arsenopyrite needles, and that Zn and Au are concentrated in the center of the cluster of sulfide C. 3 µm resolution SR-XRF mapping shows that there are chalcopyrite grains in the centre and that the groundmass is Ca and Mn rich.

sulfide content is dominated by arsenopyrite, which occurs as small clusters of needles at the margins of quartz-carbonate stringers, large mm scale clusters associate (Fig. 3a inset), and as elongated needles. The large clusters of arsenopyrite are associated with fine-grained chalcopyrite, sphalerite, and gold (Fig. 3b). Coarse sample mapping also identified gold on the < 15 µm scale associated with the larger clusters of arsenopyrite. Fine-scale mapping (8 and 2 µm resolution; Fig. 3b, c) reveals that the arsenopyrite needles are uniform in their geochemistry on the micron scale, with no core-rim structures or growth haloes (Fig. 3b, c). Small Ni-rich grains (likely pentlandite) occur throughout the arsenopyrite cluster (Fig. 3b) and Cu and Zn are concentrated at the center of the cluster, which does not contain arsenopyrite. Fine-grained gold also occurs in the central region of the cluster, which is also Ca and Mn (carbonate- rich (Fig. 3b, c). The arsenopyrite raw spectra extracted from the maps indicates that there is no refractory gold in the arsenopyrite.

4.2.2. Sample C408780

Sample C408780, a sulfide-rich and auriferous interflow sediment (C408780) is crosscut by a small cm = scale carbonate (ankerite) vein, and contains variable sulfide content dominated by pyrite and sphalerite. Coarse 20 µm resolution mapping reveals the sample also contains fine-grained arsenopyrite and chalcopyrite associated with the ankerite veinlet. Two different associations with gold and trace metals (Au-Zn and Au-Cu-pyrite) are identified and highlighted in inset boxes, and gold is not related to a crosscutting ankerite veinlet (Fig. 4a). The most spectacular gold mineralization style observed is free gold (20–200 µm scale) associated with coarse-grained subhedral to euhedral pyrite, massive sphalerite and fine-grained arsenopyrite mineralization (Fig. 4b). The second type of gold mineralization occurs as ~20 µm inclusions in euhedral pyrite with associated pyrrhotite and chalcopyrite mineralization. These euhedral pyrite grains contain Ni and show some zonation in their As content with As-rich rims (Fig. 4c).

4.2.3. Sample C406934

The ankerite vein samples is dominated by ankerite and calcite with minor quartz. The sample contains disseminated pyrite which is concentrated towards the vein margin (top of sample). 20 µm resolution mapping (Fig. 5a) reveals that gold is associated with regions of pyrite mineralization in the carbonate-rich vein material and that many grains have As-rich cores (Fig. 5a). Gold in the vein material occurs primarily in the main ankerite vein material. Gold occurs with fine- and coarse-grained pyrite, in pyrite stringers as well as with disseminated pyrite. High-resolution (3 µm) SR-XRF mapping of a gold-bearing pyrite grain shows that gold occurs along the pyrite grain margin and in fractures (Fig. 5b). It also reveals complex zonation of As and trace metals (Cu, Zn, Ni) which occurs both as laminations and inclusions, which are Cu- and As-rich. Depletions in S are also observed in some of the As enriched haloes. At the grain-scale, the As content of the glass slide does not interfere with mapping as the density of pyrite does not allow for X-

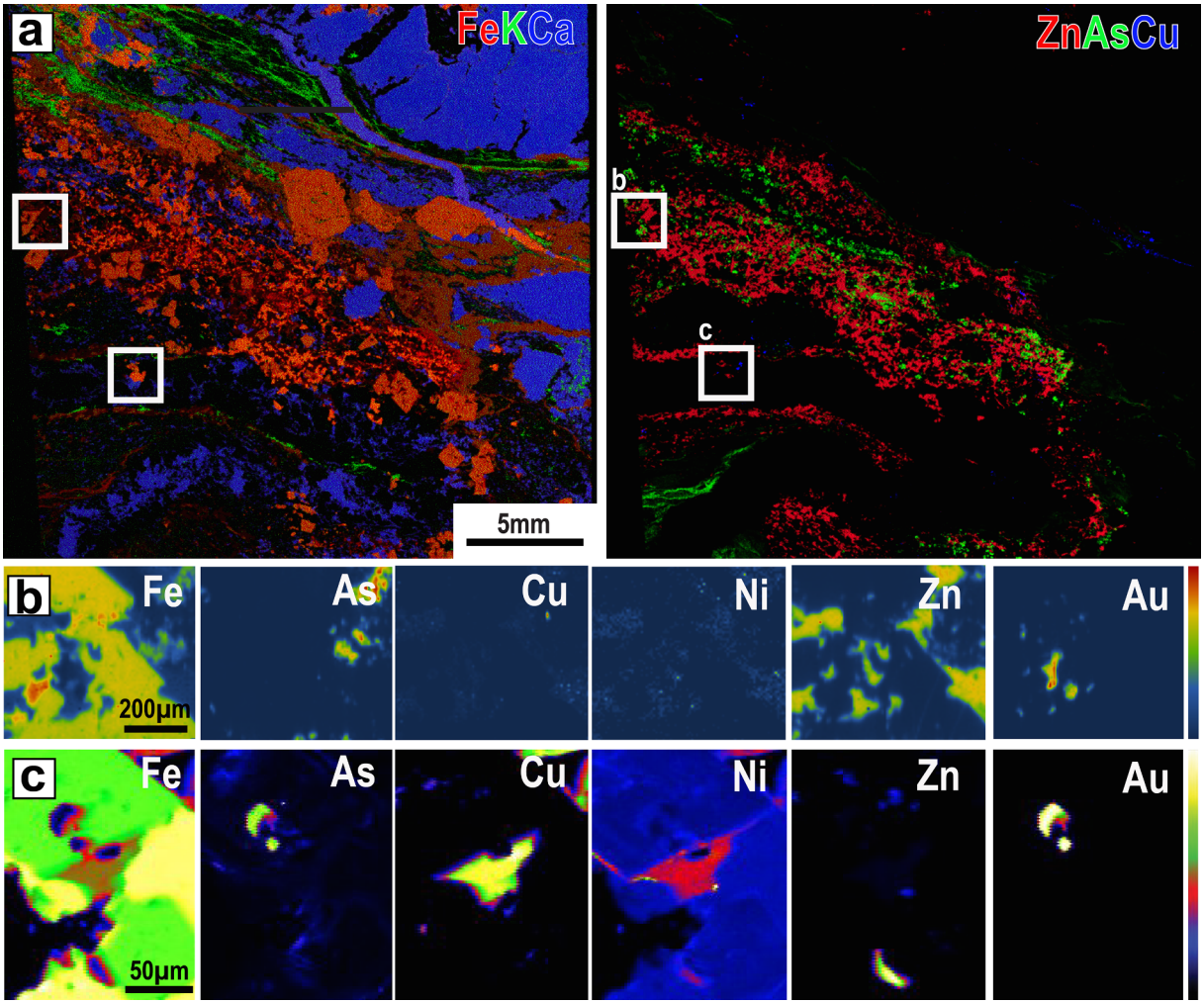

Fig. 4. SR-XRF maps of samples C408781. A. 20 µm resolution RGB maps of a thin section mounted on a quartz slide reveal the textural relationships between several styles of sulfide mineralization as well as overprinting veining. B. 8 µm resolution mapping shows an example of free gold associated with pyrite and sphalerite mineralisation C. 2 µm resolution SR-XRF of a euhedral pyrite grain with a gold inclusion.

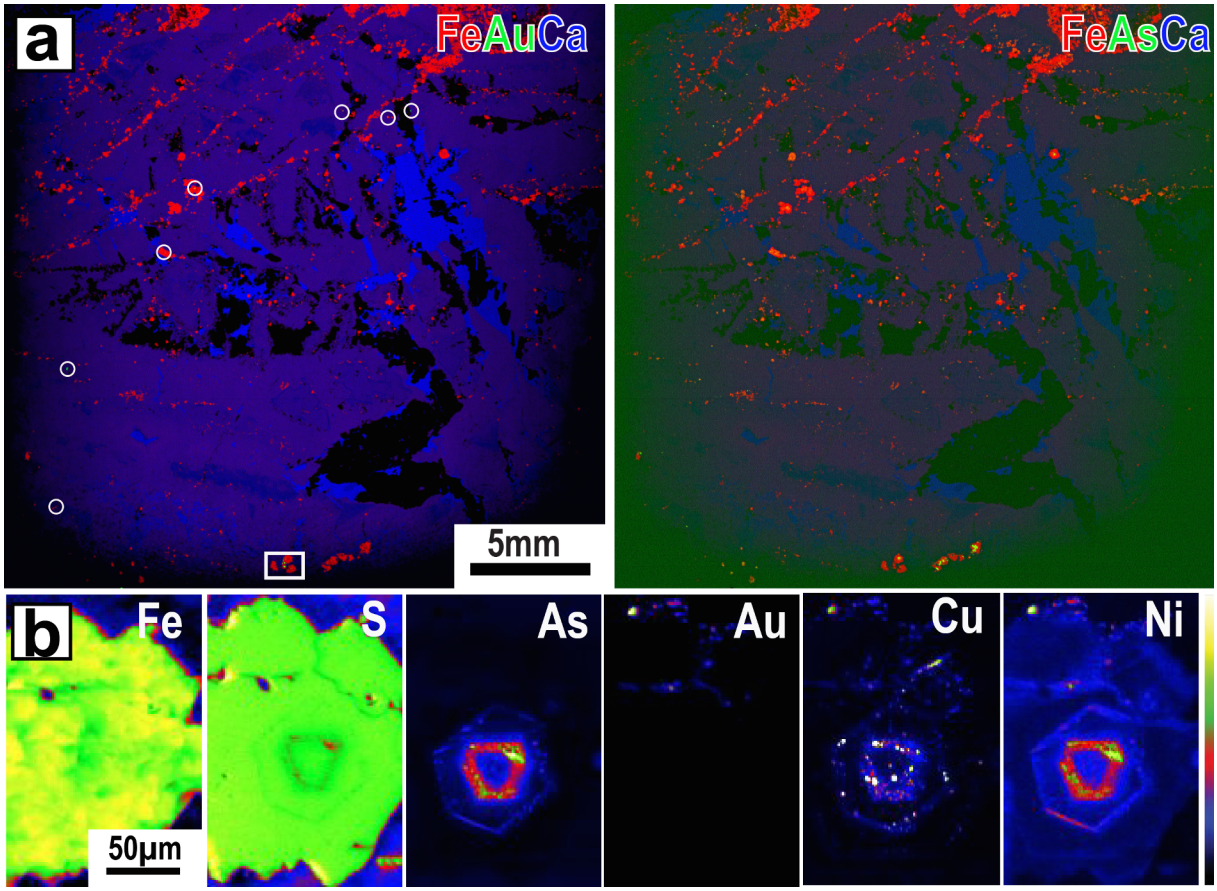

Fig. 5. A. SR-XRF maps of sample C406934. A. 20 µm resolution RGB maps of a thin section of gold bearing ankerite vein show the distribution of pyrite in the ankerite rich vein material. The circles outline regions with Au mineralization, and the square is the region mapped in B. High resolution SR-XRF maps (2 µm resolution) show complex zonation of As, Cu, Zn and Ni in the pyrite grain (C406934_001) as well as Au at grain margins and in fractures. The thin section is mounted on conventionally used float glass, and the As content of the glass interferes with sample scale mapping in regions which are not sulfide rich.

ray penetration through the ~30 µm thick pyrite grain to the glass, and the high As content of the arsenian pyrite overshadows any As detected in the glass through the carbonate-rich groundmass (Fig. 5b).

4.2.4. Sample C408779

Sample C408779 is an auriferous sulfide clast dominated by subhedral to euhedral pyrite with minor chalcopyrite. Mapping of a thin section and its corresponding billet off cut reveals pyrite grains with As-rich rims and inner haloes, and that gold occurs at pyrite grain margins. (Fig. 6a, d). At the sample scale, whole rock mapping provides better resolution for As mapping and better reveals As-rich growth haloes because there is no interference from the thin section glass (Fig. 6d). Higher resolution mapping (10 µm resolution) reveals euhedral Ni zonation in the pyrite grains, which was not resolvable at the sample-scale. It also reveals the textural relationships between sphalerite, chalcopyrite and pyrite mineralization (Fig. 6b, e). Multi-stage pyrite growth was investigated further with 2 µm resolution mapping (Fig. 6e, f) and reveals that in addition to As and Ni zonation, the pyrite grain has a copper enriched anhedral core. This is overprinted by arsenian euhedral overgrowth with a Ni enriched euhedral rim. In the whole rock sample, topography begins to impact mapping at the 2 µm scale, however, the trace element associations observed in thin section mapping are still resolvable (Fig. 6e, f).

4.3. Point XRF and XANES

4.3.1. Sample C406934

A transect of XRF spectra across the As-rich halo in the Au- and As-rich grain in sample C406934 (Fig. 5b) reveals that even the As-poor regions of the map have substantial As content (Fig. 7a, b). It also reveals a negative correlation between the concentration of As and Fe in the sample as you move out from the grain center providing insights into the mode of As uptake into the pyrite lattice. Point SR-XRF also identifies a minor refractory gold contribution, which is highest in the outer As halo of the grain as evidenced by a peak at ~9713 eV (Au Kα) (Fig. 7a).

The XANES spectra across the same transect reveals a change in As speciation as you move across the halo to the rim of the pyrite grain (Fig. 7c). Arsenic in outer halo has a XANES spectrum dominated by an edge position characteristic of As^{1-} (11,867 eV) that is commonly observed in arsenopyrite and arsenian pyrite. There is contribution of more than one As species in the inner halo and the outer rim of the grain (Fig. 7b). The outer rim of the grain contains less As, but has a XANES spectrum characteristic of more oxidized As species with features at 11,871 eV (As^{+3}) and 11,874 eV (As^{5+}). The shape of the Au L-edge XANES spectrum (Fig. 7d) of Au from the Au-rich region of the transect (Fig. 7a) is consistent with the presence of metallic Au^0 and Au^{1+}. This indicates that the there is a refractory gold contribution from lattice bound gold, as well as metal nano-particulate gold in that region of the grain.

SR-XRF map stacks were collected to visualize the spatial variability in As speciation across the grain at the 20 µm scale. The average XANES spectra for the entire region reveals that As^{1-} as the dominant As species in the pyrite grain, with an edge position of 11,867 eV (Fig. 8). This reflects the fact that the bulk of the As in the sample is from the As-rich core of the grain (Fig. 7a, b). The contribution of As from the As poor

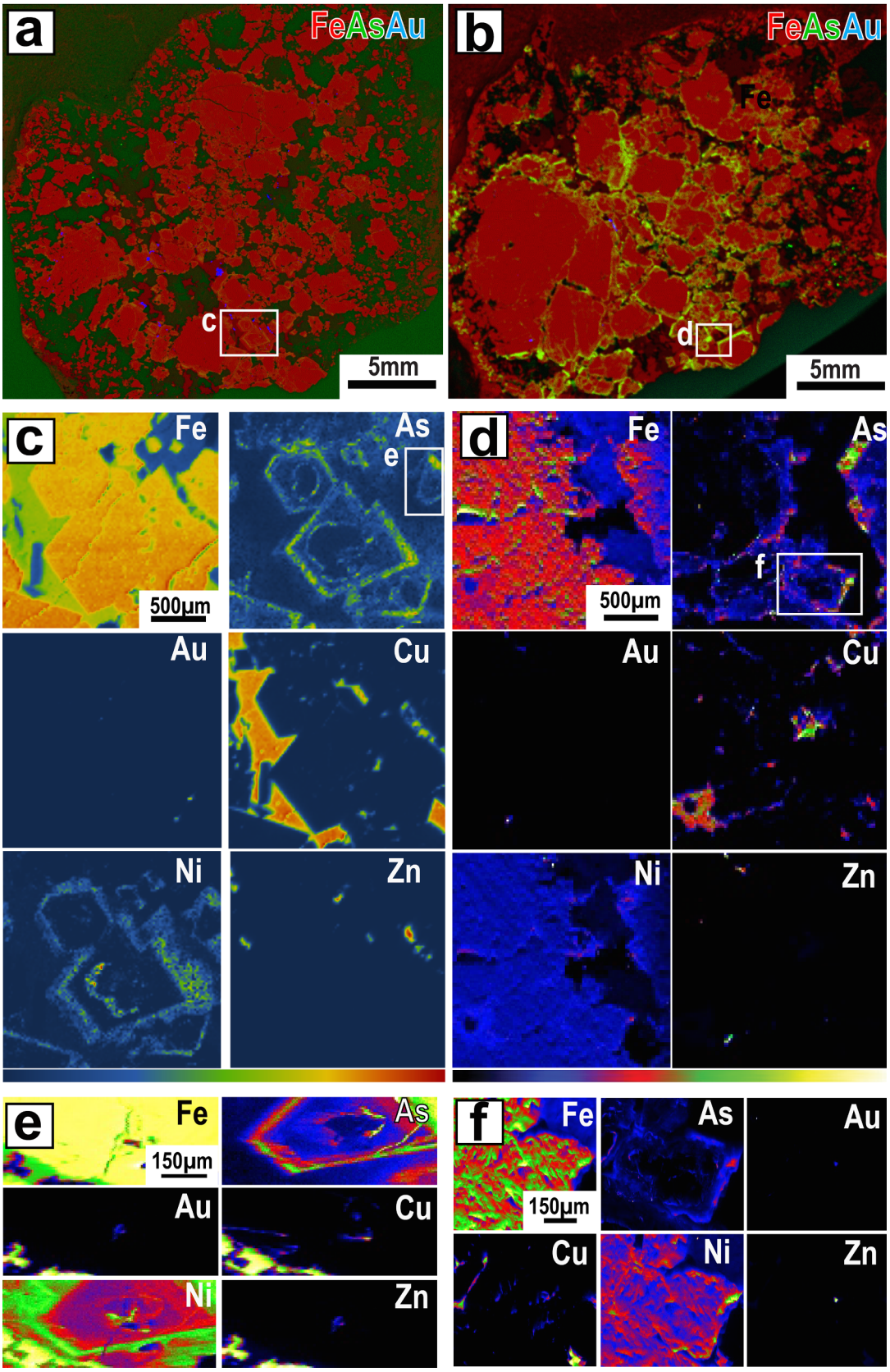

Fig. 6. SR-XRF mapping of C408779 thin section and billet. A and D. RGB maps at 20 µm resolution show that there is zonation in the As contents of pyrite grains, and gold at grain margins. However, zonation in the pyrites is more pronounced in the raw rock sample due to the As content of the glass slide on which the thin section is made. B and E. At a slightly higher resolution (B-8 µm resolution) and more zoomed in (E-20 µm resolution) SR-XRF maps from the CLS (B) and APS (E) show that there is also a bimodal spatial relationship between As and Ni pyrite content. C. and F. At 2 µm resolution, the relationship between Au and Ni can be clearly seen and sample topography begins to have an influence on map quality (C- C408779_001).

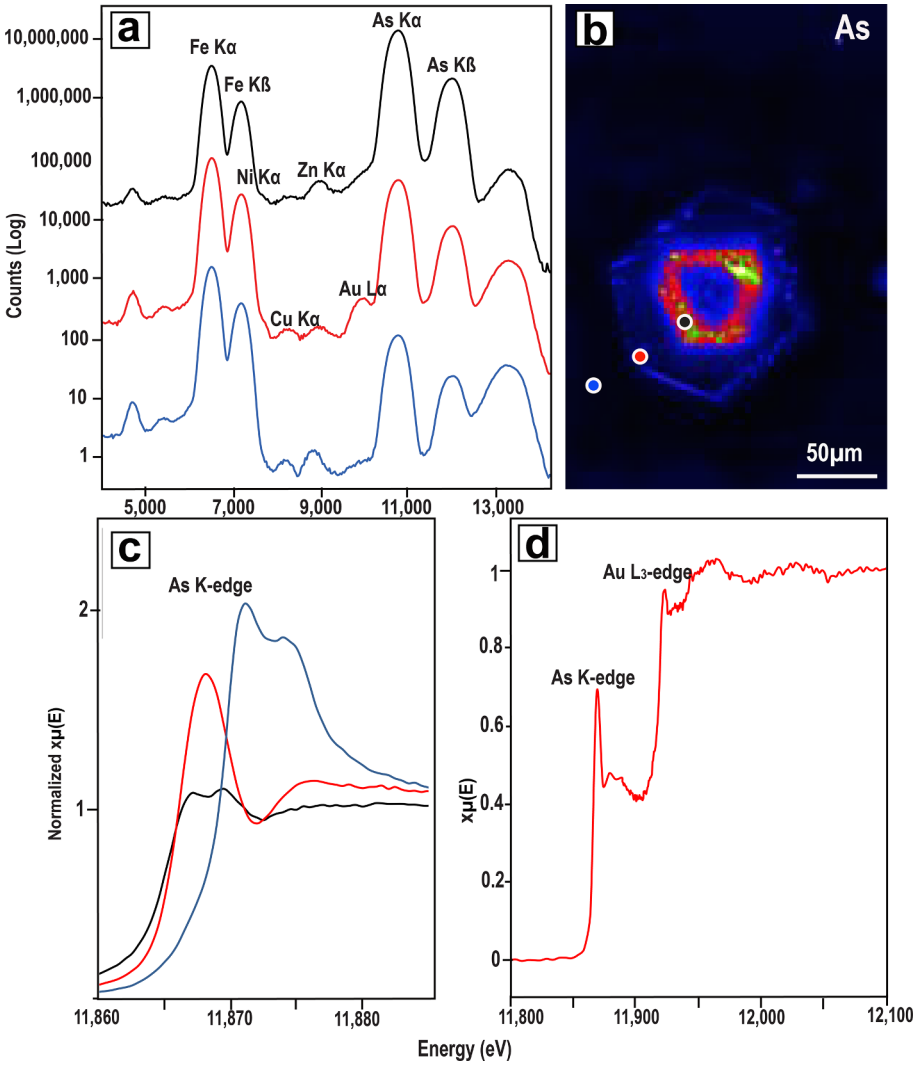

Fig. 7. SR-XRF and XANES spectrum of C406934_001. A SR-XRF spectrum across a haloed grain show variability in As and trace metal content. The black and blue spectra are displaced for clarity. B. Map of As content (Fig. 5) showing the positions from which point SR-XRF and XANES data was collected (spots). C. Normalized spectra of the As-K edge region shows differences in edge position and shape indicating changes in As speciation across the grain. D. Au-L edge XANES spectra for the outer As halo which showed Au in the XRF spectra.

regions at the edge of the grain is negligible in terms of total grain As. A limiting factor is the 20 µm spatial resolution of the map, which is not sufficient to visualize the fine growth haloes. The map also highlights the issue of using glass slides, as the contribution of As^{3+} and As^{5+} from the glass can be detected in the 11,871 and 11,874 eV maps (see Supplementary materials for glass XANES spectra). This is observed as the lighter blue region around the grain where the X-rays can penetrate the carbonate groundmass to sample the glass.

4.3.2. Sample C408779

A transect of point SR-XRF analysis across the pyrite grain from the rim to the core in Fig. 6e (Fig. 9a), shows variability in the As and trace metal contents (Cu, Ni, Zn) across the grain but no detectable gold (Fig. 9b). The core of the grain is enriched in Zn whereas the rim is enriched in Ni, Cu and As (Fig. 9a, b). XANES analyses were taken from the same locations and reveal variability in the speciation of As across the grain. The XANES spectra from the As-rich rim of the grain are characteristic of As^{1-} with an edge position of 11,867 eV (Fig. 9c). The As-K edge of the XANES spectra from the poor inner region of the grain is at a higher energy than the rim spectra (Fig. 9c). The feature at 11.871 eV is characteristic of a more oxidized form of As, likely As^{3+}. SR-XRF map stacks were collected and confirm the presence of As^{1-} as the dominant As species in the pyrite grain, with an edge position of 11,867 eV (Fig. 10). However, it is apparent that in the central regions of the pyrite grain the edge shifts to slightly higher energy with a change in edge shape that reflecting the observations made in the point spectra.

4.4. Whole rock mapping

The capability of whole rock mapping to provide meaningful geochemical information for previously uncharacterized samples was investigated with 20 µm resolution SR-XRF mapping (Fig. 11). Two samples from different deposits and host rock are described in more detail below.

4.4.1. Buffalo ankerite (BA)

Sample BA is an ankerite vein sample from the Buffalo Ankerite mine hosted in an ultramafic (komatiite) volcanic unit. The sample is dominated by quartz, ankerite, sericite, and pyrite. Mapping reveals that the much of pyrite in the sample is arsenian in nature and is associated with fine-grained arsenopyrite (Fig. 12). It also identifies the presence of fine-grained Ni sulfides and an association between intense sericitization (K map), Ni and and pyrite. Gold in the sample occurs

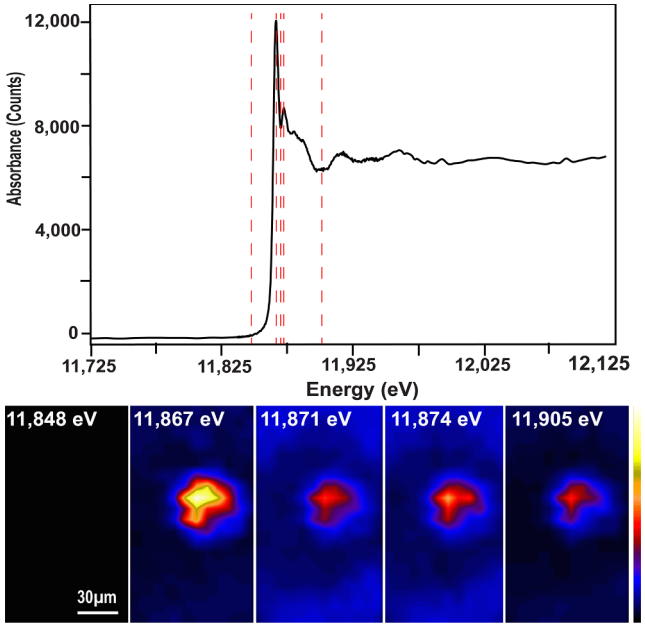

Fig. 8. SR-XRF As XANES stacks of C406934_001 (Fig. 5). Average As XANES spectra of a haloed pyrite grain (20 µm resolution) and As maps at multiple energies. The As K-edge is indicative of As^{1+} being the primary species of As in the pyrite grain.

associated with pyrite (top of sample) as well as fine-grained Ni sulfides (bottom right), and with the region of intense sericitization in the center of the sample.

4.4.2. Sample C410901

Mapping of a whole rock sample of ankerite veinlet in an unmineralized outcrop of Tisdale Assemblage reveals variability in ankerite chemistry (Fig. 13 Fe, Ca, Mn maps). The sample is dominated by banded ankerite with quartz extension veins and fine-grained disseminated pyrite at the vein margin. Mapping also reveals the presence of arsenopyrite, chalcopyrite and a fine-grained T- bearing phase (likely rutile) in the wall rock. Arsenopyrite is associated with the ankerite veinlet margin but also a quartz stringing in the wall rock. Gold is only conclusively detected as one small occurrence of free gold in the wall rock (Fig. 13).

5. Discussion

SR-XRF mapping of samples is an effective method for quickly and effectively identifying the presence of gold in multiple types of complex ore samples, for characterizing gold associations with various mineral phases, and for identification of trace element associations with gold. This is an inherently time consuming task by conventional petrographic methods as gold in orogenic deposits is commonly nuggetty on the sample and micrometer scale. We show that it is possible to quickly and efficiently detect and characterize gold in heterogeneous and complex samples from multiple depositional contexts. If this information is available early in the mining cycle it could be used to guide exploration in complex systems where bulk rock geochemistry does not provide clear trace element associations or vectors towards mineralization, and can also provide insights into future remediation and geometallurgical issues.

5.1. Multi-scale mapping

High-resolution *in situ* trace element mapping of pyrite has become an increasingly important part of ore deposit research (e.g., Large et al., 2009; Fougerouse et al., 2016; Sykora et al., 2018). Mapping of auriferous grains in sample C407932 (Fig. 2) shows that SR-XRF and EPMA produce equivalent datasets in terms of spatial resolution and detectability of trace metals. EPMA and LA-ICP-MS are broadly used in the mining industry for grain-scale studies, and they rely on extensive sample characterization by traditional methods (petrography, BSE-SEM) for grain selection (e.g., Fig. 2). This is due to limitations in the scale of the mappable area by EPMA, SIMS and LA-ICP-MS, as well as sample preparation requirements (Fig. 1). The ability of SR-XRF to produce large-scale maps can improve the efficiency of grain selection for higher resolution studies and mitigate sample bias by providing geochemical information on a large number of grains (e.g., Figs. 3 and 4).

The capability of SR analysis for interrogating samples at multiple scales and with multiple techniques hinges on its non-destructive nature. This also makes it very complementary to other more traditional techniques (e.g., LA-ICP-MS, SIMS, TEM). The caveat is that mounting samples on traditional thin section glass is problematic due to the trace element of the glass (e.g., Figs. 5 and 6). This is particularly important for orogenic gold deposits where As is common and often an important trace element vector for gold, but can be mitigated by using

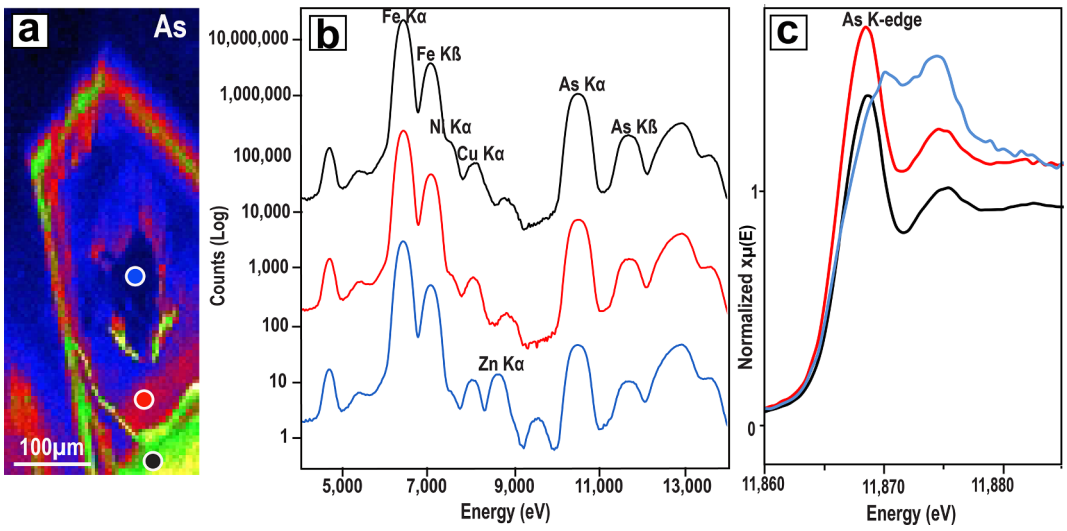

Fig. 9. SR-XRF and XANES spectra of C408779_001. A. SR-XRF map of As in grain C408779_001 (Fig. 10C) B. SR-XRF spectrum show variability in As and trace metals across the growth haloes C. The normalized edge region of the As K-edge XANES spectra reveals that rim regions of the grain are dominated by As^{1+} and the core of the grain contain As in a higher oxidation state (As^{3+} and As^{5+}).

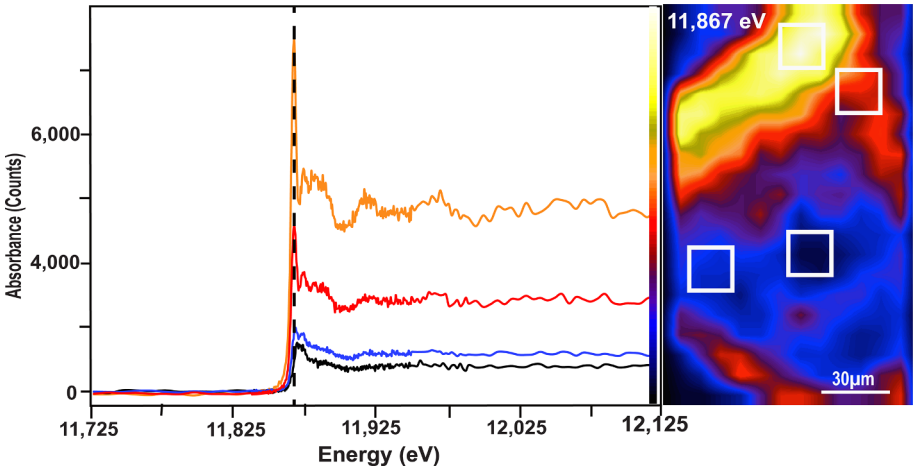

Fig. 10. XANES As stack of C408779. XANES spectra from a haloed pyrite grain in the auriferous clast, and a map at 11.867 keV (spectra extracted from regions outlined in map, and corresponding colors).

quartz slides or whole rock slabs. The four examples of multi-scale mapping highlight the ability of SR-XRF mapping of thin sections for identifying gold in heterogeneous samples from a number of different depositional contexts; greywacke (E885276), a massive sulfide lens (C408781), hydrothermal vein (C406934), and conglomerate (C408779). Gold grades range from 2.73 to 98.1 g/t in these samples and gold is nuggety and occurs on the 5–50 µm scale. SR-XRF mapping on the sample scale quickly identified gold in each sample type and provided integral mineralogical context for mineralization. Additionally, the datasets are not constrained to a small number of preselected elements of interest as with EPMA. Each pixel contains a full spectrum, which allows for further interrogation of the data and can provide insights in new and sometimes unexpected results.

Higher resolution mapping of gold-bearing regions of the samples provided insights into mineralizing mechanisms, fluid histories and trace element vectors. In sample E885276, gold is associated with arsenopyrite mineralization and not pyrite, and there is no refractory gold in the sulfide phases. In the rest of the samples, gold is generally associated with pyrite and in the case of the conglomerate pyrite clast, gold is related to the As-rich rims of pyrite grains (Fig. 6). The converse is true of the vein sample (C406934) where free gold occurs in fractures and on the vein margins of a pyrite with an As-rich core. For the synvolcanic interflow sediment samples, gold is not associated with As or overprinting carbonate veining but is more closely related to early Zn and Cu.

All the samples show evidence for multiple fluid events, and multi-scale mapping provides insights into the timing of gold introduction to the system. Gold in samples E885276 and C408781 is associated with sulfide mineralization (arsenopyrite, sphalerite, pyrite) and not overprinting veining. Both the vein (C406934) and clast (C408779) samples show evidence for multiple overprinting fluid events in the distribution of trace elements in pyrite. Pyrite grains show complex patterns of As, Ni and Cu zonation as well as textural evidence for remobilization of metals. In sample C408779, this core rim pattern is resolvable in the sample scale mapping, and is ubiquitous in the sample providing evidence post-depositional stage of hydrothermal overprinting. These pyritic clasts are some of the earliest mineralization in the Timmins camp and are described in detail by Gray and Hutchinson (2001). The mapping observations provide further evidence for the role of epigenetic upgrading and possible metamorphic recrystallization of auriferous pyrite in the pyritic clasts of the Timiskaming conglomerate. Understanding the role of variable enrichment from multiple fluid events and remobilization of metals and gold in ore systems is integral to developing exploration vectors.

Generally, *in situ* mapping techniques are labor intensive, time consuming and require extensive sample preparation and so are not utilized at the early stages of an ore deposit study or in exploration. Using sample C408779 we show that comparable datasets to prepared thin sections can be obtained using whole rock slabs. The ability to map whole rock samples with full spectrum datasets allows for the application of *in situ* geochemistry as early as the exploration stage. The application of whole rock mapping was applied to two previously uncharacterized samples (BA, C410901). Both contain less than 1 g/t in bulk sample geochemical analysis and mapping reveals free gold. This

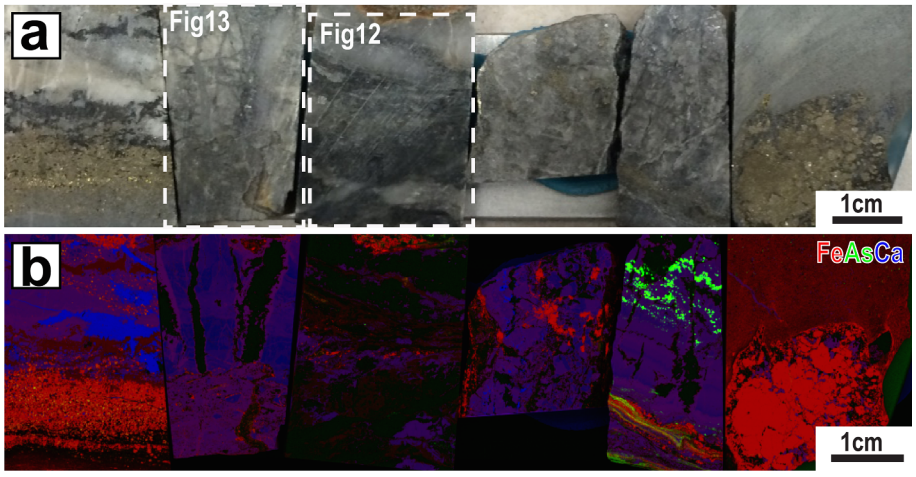

Fig. 11. Whole rock SR-XRF RGB maps A. 6 whole rock samples (C409401, C410910, BA, C410300, C410280, C408779) were mapped at 20 µm resolution over ~ 11hrs. The 5 on the left are all cut from raw samples and the far right sample is a thin section offcut (Fig. 6). B. SR-XRF maps (20 µm resolution) of 6 whole rock samples (red – Fe, green – As, blue – Ca).

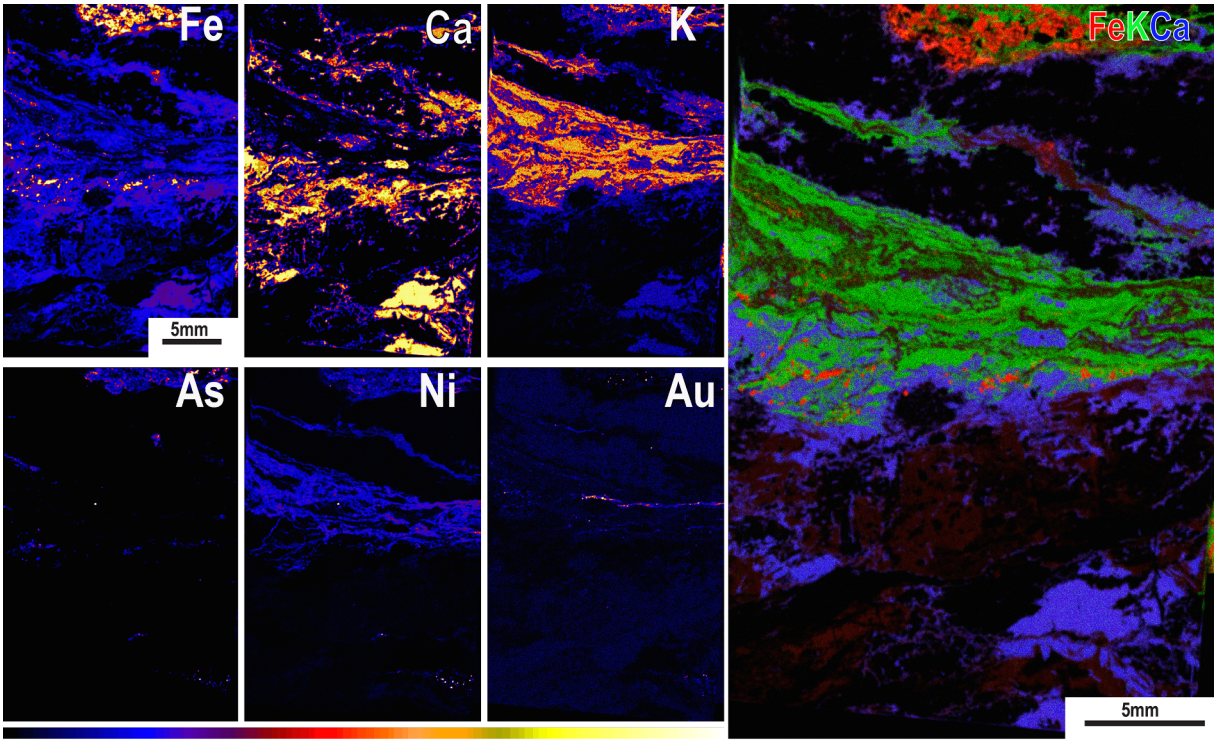

Fig. 12. Whole rock SR-XRF maps for sample BA, a raw cut sample from the Buffalo-Ankerite mine. Mapping reveals differences in the vein geochemistry of these ankerite veins from the Dome ankerite veins and provides context for gold mineralization as well as trace element information with mineralogical context samples.

highlights the nugget effect commonly encountered in sampling for orogenic gold.

5.2. Metal speciation

The non-destructive nature of, and the full spectrum datasets produced by SR-XRF mapping allows for the interrogation of a large range of trace elements and further characterization of samples of interest. In particular, the relationship speciation of As and Au in pyrite is important for orogenic gold studies in the contexts of geometallurgy and remediation. The nature and abundance of refractory gold will determine the extraction method required for ore processing and impact gold recoveries, and the nature of As in the ore samples has important environmental consideration.

In the case of the arsenopyrite-rich greywacke (E885276) sample, the relationship between gold and arsenopyrite was constrained by multi-scale mapping and a suspected component of refractory gold was ruled out by investigating the XRF spectrum. Conversely, refractory gold was identified in a discrete region of As-rich halo of a zoned pyrite grain in sample C406934 (Fig. 7). Further analysis by XANES was applied to distinguish whether the refractory gold is nano-particulate metallic gold or lattice bound Au^{1+} and indicated that both forms were present. While in these examples the refractory gold content of the sample is negligible, it serves as an example of the application of this techniques to other deposits where there may be significant implications for ore processing and improving recoveries based on the presence of lattice bound gold, which may require high-pressure oxidation of the pyrite for liberation.

Understanding the relationship between Au and As is also relevant for exploration and remediation. It can provide insights into fluid chemistry, metal endowments and mineralizing mechanisms and the potential for metal release into the environment. Samples C406934 (Fig. 5) and C408779 (Fig. 6) show evidence for multiple stages of pyrite growth in their SR-XRF mapping. The speciation of As in the zoned pyrites was investigated by XANES to provide insights in to the redox state of the mineralizing fluids. XANES point analysis transects show a converse change in As speciation from the pyrite core to rim in the two samples. The vein sample has an As^{1-}-rich core and a rim in which the As is in its more oxidized states ($As^{3+/5+}$). Generally As occurs in pyrite as As^{1-}, but under more oxidizing conditions pyrite will incorporate As^{3+} into its structure (Reich et al., 2005; Deditius et al., 2008, 2014). The speciation of As can reveal changes in the redox conditions of the fluid, which may play a role in the concentration of deleterious elements and gold in pyrite (Deditius et al., 2008). The SR-XRF stacks applied to samples C406934 (Fig. 8) and C408779 (Fig. 10) are limited in their spatial resolution, however, they provide a useful measurement of the bulk As speciation of the samples. Despite the variable observed in both samples on the micron scale, they are dominated by As^{1-}. Traditionally, these sorts of speciation studies have only been applied late in the mining cycle to address environmental and remediation questions. However, with advances in the application of SR-XRF stacks, it is possible to investigate trace element speciation on the sample scale and provide insights in the distribution of refractory gold and deleterious elements early in the mine cycle to identify potential future remediation and geometallurgical issues.

6. Conclusions

This work highlights the potential for improving the speed and workflow for high-resolution studies of ore deposits while providing simultaneous geochemical and textural datasets which exceeds conventional methods. Integrating bulk rock with *in situ* multi-scale synchrotron analysis provides a very powerful dataset in which the micron-scale geochemical observations are well constrained and can be more confidently extrapolated to the sample or deposit scale. The value of moving beyond simple bulk rock geochemistry early in the mine cycle is being addressed by the scientific community (e.g., QEMSCAN, Terraspec, table top XRF systems). However, none of the techniques presently available provide the same spatially resolvable, multi-scale, and quantitative geochemical information as SR-XRF mapping does.

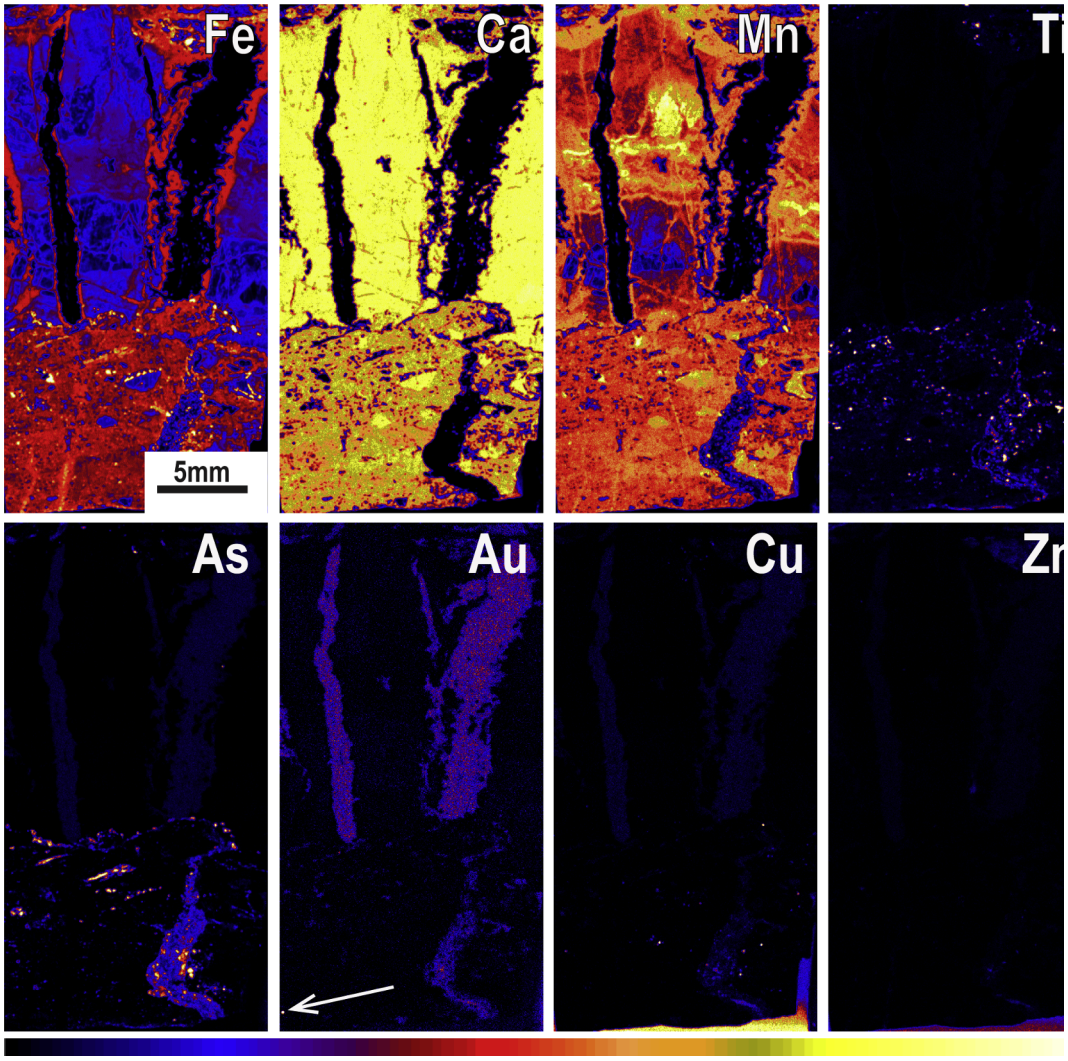

Fig. 13. SR-XRF maps C410910, a raw cut sample from Pearl Lake. Mapping reveals variations in the geochemistry of vein mineralogy (carbonate Fe and Mn content), trace metal content of sulfide phases (As, Cu) and identifies micrometer scale gold mineralization throughout the sample.

The integration of large-scale SR-XRF mapping datasets at the beginning of a workflow (on whole rock samples) followed by higher resolution mapping, point SR-XRF and XANES analysis has not been previously described for orogenic systems. The lack of sample preparation required for these techniques makes them ideal for integration into standard exploration and metallurgical studies early in the mining cycle. This is integral to avoiding mineral liberation issues in the future of a deposit, and for exploring in a climate in which lower grade and more complex deposit types are being exploited. This workflow is not just relevant for orogenic deposits but can be applied to any deposit type in which ore minerals and elements are dilute.

Acknowledgments

We would like to acknowledge the support of Goldcorp Porcupine Gold Mines for their support of this research, and in particular the geology engineering departments at the Dome Mine. We thank the support and beam line staff at the Advanced Photon Source (Zou Frinfrock), Cornell High Energy Synchrotron Source (Louisa Smeiska), and Canadian Light Source (Peter Blanchard) synchrotron facilities. The reviewers (Martin Reich, Nicolas Thebaud, and anonymous) are thanked for their feedback during the revision process. This research was financially supported by Goldcorp, the National Science and Engineering Research Council of Canada, the Ontario Centers of Excellence, and the Society of Economic Geologists Canada Foundation.

Appendix A. Supplementary data

Supplementary data to this article can be found online at https://doi.org/10.1016/j.oregeorev.2018.11.015.

References

Bancroft, G.M., Hyland, M.M., 1990. Spectroscopic studies of adsorption/reduction reactions of aqueous metal complexes on sulphide surfaces. Rev. Mineral. Geochem. 23 (1), 511–558.

Barnes, S.J., Le Vaillant, M., Lightfoot, P.C., 2017a. Textural development in sulfide-matrix ore breccias in the Voisey's Bay Ni-Cu-Co deposit, Labrador, Canada. Ore Geol. Rev. 90, 414–438.

Barnes, S.J., Mungall, J.E., Le Vaillant, M., Godel, B., Lesher, C.M., Holwell, D., Lightfoot, P.C., Krivolutskaya, N., Wei, B., 2017b. Sulfide-silicate textures in magmatic Ni-Cu-PGE sulfide ore deposits: disseminated and net-textured ores. Am. Mineral. 102 (3), 473–506.

Blanchard, P.E., Van Loon, L.L., Reid, J.W., Cutler, J.N., Rowson, J., Hughes, K.A., Brown, C.B., Mahoney, J.J., Xu, L., Bohan, M., Demopoulos, G.P., 2017. Investigating arsenic speciation in the JEB Tailings Management Facility at McClean Lake, Saskatchewan using X-ray absorption spectroscopy. Chem. Geol. 466 (4), 617–626.

Brown, G.E., 1990. Spectroscopic studies of chemisorption reaction mechanisms at oxide-water interfaces. Rev. Mineral. Geochem. 23 (1), 309–363.

Brugger, J., Pring, A., Reith, F., Ryan, C., Etschmann, B., Liu, W., O'Neill, B., Ngothai, Y., 2010. Probing ore deposits formation: new insights and challenges from synchrotron and neutron studies. Radiat. Phys. Chem. 79 (2), 151–161.

Cabri, L.J., Newville, M., Gordon, R.A., Crozier, E.D., Sutton, S.R., McMahon, G., Jiang,

D.T., 2000. Chemical speciation of gold in arsenopyrite. Can. Mineral. 38 (5), 1265–1281.
Campbell, S.G., Reith, F., Etschmann, B., Brugger, J., Martinez-Criado, G., Gordon, R.A., Southam, G., 2015. Surface transformations of plantinum grains from Fifield, New South Wales, Australia. Am. Mineral. 100, 1236–1243.
Cook, N.J., Chryssoulis, S.L., 1990. Concentrations of invisible gold in the common sulfides. Can. Mineral. 28 (1), 1–16.
Cook, N.J., Ciobanu, C.L., Meria, D., Silcock, D., Wade, B., 2013. Arsenopyrite-pyrite association in an orogenic gold ore: tracing mineralization history from textures and trace elements. Econ. Geol. 108 (6), 1273–1283.
Deditius, A.P., Utsunomiya, S., Renock, D., Ewing, R.C., Ramana, C.V., Becker, U., Kesler, S.E., 2008. A proposed new type of arsenian pyrite: composition, nanostructure and geological significance. Geochim. Cosmochim. Acta 72 (12), 2919–2933.
Deditius, A.P., Utsunomiya, S., Reich, M., Kesler, S.E., Ewing, R.C., Hough, R., Walshe, J., 2011. Trace metal nanoparticles in pyrite. Ore Geol. Rev. 42 (1), 32–46.
Deditius, A.P., Reich, M., Kesler, S.E., Utsunomiya, S., Chryssoulis, S.L., Walshe, J., Ewing, R.C., 2014. The coupled geochemistry of Au and As in pyrite from hydrothermal ore deposits. Geochim. Cosmochim. Acta 140, 644–670.
Dimov, S.S., Hart, B.R., 2011. Applications of Microbeam Analytical Techniques in Gold Deportment Studies. In: Deschenes, G., Dimatrikapoulis, R., Bouvhard, J. (Eds.). Proceedings of the 50th Annual Conference of Metallurgists of CIM, World Gold 2011. pp. 17–26.
Dyar, M.D., Delaney, J.S., Sutton, S.R., 2001. Fe XANES spectra of iron-rich micas. Eur. J. Mineral. 13 (6), 1079–1098.
Etschmann, B.E., Ryan, C.G., Brugger, J., Kirkham, R., Hough, R.M., Moorhead, G., Siddons, D.P., De Geronimo, G., Kuczewski, A., Dunn, P., Paterson, D., 2010. Reduced As components in highly oxidized environments: evidence from full spectral XANES imaging using the Maia massively parallel detector. Am. Mineral. 95 (5–6), 884–887.
Etschmann, B.E., Donner, E., Brugger, J., Howard, D.L., de Jonge, M.D., Paterson, D., Naidu, R., Scheckel, K.G., Ryan, C.G., Lombi, E., 2014. Speciation mapping of environmental samples using XANES imaging. Environ. Chem. 11 (3), 341–350.
Etschmann, B., Liu, W., Li, K., Dai, S., Reith, F., Falconer, D., Kerr, G., Paterson, D., Howard, D., Kappen, P., Wykes, J., 2017. Enrichment of germanium and associated arsenic and tungsten in coal and roll-front uranium deposits. Chem. Geol. 463, 29–49.
Fawcett, S.E., Jamieson, H.E., 2011. The distinction between ore processing and post-depositional transformation on the speciation of arsenic and antimony in mine waste and sediment. Chem. Geol. 283 (3), 109–118.
Feick, K., 2016. An Evaluation of the Lithologies and Geochemistry of the Upper Beaver Deposit of the Kirkland Lake Area. University of Western Ontario.
Fenter, P.A. (Ed.), 2002. Applications of synchrotron radiation in low-temperature geochemistry and environmental sciences. Geochemical Society.
Fisher, L.A., Fougerouse, D., Cleverley, J.S., Ryan, C.G., Micklethwaite, S., Halfpenny, A., Hough, R.M., Gee, M., Paterson, D., Howard, D.L., Spiers, K., 2015. Quantified, multi-scale X-ray fluorescence element mapping using the Maia detector array: application to mineral deposit studies. Miner. Deposita 50 (6), 665–674.
Fougerouse, D., Micklethwaite, S., Tomkins, A.G., Mei, Y., Kilburn, M., Guagliardo, P., Fisher, L.A., Halfpenny, A., Gee, M., Paterson, D., Howard, D.L., 2016. Gold remobilisation and formation of high grade ore shoots driven by dissolution-reprecipitation replacement and Ni substitution into auriferous arsenopyrite. Geochim. Cosmochim. Acta 178, 143–159.
Gray, M.D., Hutchinson, R.W., 2001. New evidence for multiple periods of gold emplacement in the Porcupine mining district, Timmins area, Ontario, Canada. Econ. Geol. 96 (3), 453–475.
Jones, M.P., 1987. Applied Mineralogy: A Quantitative Approach. Graham & Trotman.
Kirkham, R., Dunn, P.A., Kuczewski, A.J., Siddons, D.P., Dodanwela, R., Moorhead, G.F., Ryan, C.G., De Geronimo, G., Beuttenmuller, R., Pinelli, D., Pfeffer, M., 2010. The Maia spectroscopy detector system: engineering for integrated pulse capture, low-latency scanning and real-time processing. AIP Conf. Proc. 1234 (1), 240–243.
Large, R.R., Danyushevsky, L., Hollit, C., Maslennikov, V., Meffre, S., Gilbert, S., Bull, S., Scott, R., Emsbo, P., Thomas, H., Singh, B., 2009. Gold and trace element zonation in pyrite using a laser imaging technique: implications for the timing of gold in orogenic and Carlin-style sediment-hosted deposits. Econ. Geol. 104 (5), 635–668.
Large, R.R., Bull, S.W., Maslennikov, V.V., 2011. A carbonaceous sedimentary source-rock model for Carlin-type and orogenic gold deposits. Econ. Geol. 106 (3), 331–358.
Large, R.R., Halpin, J.A., Danyushevsky, L.V., Maslennikov, V.V., Bull, S.W., Long, J.A., Gregory, D.D., Lounejeva, E., Lyons, T.W., Sack, P.J., McGoldrick, P.J., 2014. Trace element content of sedimentary pyrite as a new proxy for deep-time ocean–atmosphere evolution. Earth Planet. Sci. Lett. 389, 209–220.
Large, R.R., Mukherjee, I., Gregory, D.D., Steadman, J.A., Maslennikov, V.V., Meffre, S., 2017. Ocean and atmosphere geochemical proxies derived from trace elements in marine pyrite: implications for ore genesis in sedimentary basins. Econ. Geol. 112 (2), 423–450.
Li, K., Etschmann, B., Rae, N., Reith, F., Ryan, C.G., Kirkham, R., Howard, D., Rosa, D.R., Zammit, C., Pring, A., Ngothai, Y., 2016. Ore petrography using megapixel X-ray imaging: rapid insights into element distribution and mobilization in complex Pt and U-Ge-Cu ores. Econ. Geol. 111 (2), 487–501.
Liu, W., Mei, Y., Etschmann, B., Brugger, J., Pearce, M., Ryan, C.G., Borg, S., Wykes, J., Kappen, P., Paterson, D., Boesenberg, U., 2017. Arsenic in hydrothermal apatite: Oxidation state, mechanism of uptake, and comparison between experiments and nature. Geochim. Cosmochim. Acta 196, 144–159.
Manceau, A., Marcus, M.A., Tamura, N., 2002. Quantitative speciation of heavy metals in soils and sediments by synchrotron X-ray techniques. Rev. Mineral. Geochem. 49 (1), 341–428.
Mavrogenes, J.A., Berry, A.J., Newville, M., Sutton, S.R., 2002. Copper speciation in vapor-phase fluid inclusions from the Mole Granite, Australia. Am. Mineral. 87 (10), 1360–1364.
McIntyre, N.S., Sherry, N., Fuller, M.S., Feng, R., Kotzer, T., 2010. X-Ray fluorescence spectroscopy and mapping using excitation from white and broad bandpass synchrotron radiation. J. Anal. At. Spectrom. 25 (9), 1381–1389.
Mukherjee, I., Large, R., 2017. Application of pyrite trace element chemistry to exploration for SEDEX style Zn-Pb deposits: McArthur Basin, Northern Territory, Australia. Ore Geol. Rev. 81, 1249–1270.
Palenik, C.S., Utsunomiya, S., Reich, M., Kesler, S.E., Wang, L., Ewing, R., 2004. "Invisible" gold revealed: direct imaging of gold nanoparticles in a Carlin-Type deposit. Am. Mineral. 89, 1359–1366.
Pearce, M.A., Godel, B.M., Fisher, L.A., Schoneveld, L.E., Cleverley, J.S., Oliver, N.H., Nugus, M., 2017. Microscale data to macroscale processes: a review of micro-characterization applied to mineral systems. Geological Society, Special Publications, London, pp. 453.
Petruk, W., 2000. Applied Mineralogy in the Mining Industry. Elsevier.
Ravel, B., Newville, M.A.T.H.E.N.A., 2005. ATHENA, ARTEMIS, HEPHAESTUS: data analysis for X-ray absorption spectroscopy using IFEFFIT. J. Synchrotron Radiat. 12 (4), 537–541.
Reich, M., Kesler, S.E., Utsunomiya, S., Palenik, C.S., Chryssoulis, S.L., Ewing, R.C., 2005. Solubility of gold in arsenian pyrite. Geochim. Cosmochim. Acta 69 (11), 2781–2796.
Reich, M., Large, R., Deditius, A.P., 2017. New advances in trace element geochemistry of ore minerals and accessory phases. Ore Geol. Rev. 81, 1215–1217.
Ryan, C.G., Kirkham, R., Hough, R.M., Moorhead, G., Siddons, D.P., De Jonge, M.D., Paterson, D.J., De Geronimo, G., Howard, D.L., Cleverley, J.S., 2010. Elemental X-ray imaging using the Maia detector array: the benefits and challenges of large solid-angle. Nucl. Instrum. Meth. Phys. Res. Sect. A. 619 (1), 37–43.
Ryan, C.G., Siddons, D.P., Kirkham, R., Dunn, P.A., Kuczewski, A., Moorhead, G., De Geronimo, G., Paterson, D.J., De Jonge, M.D., Hough, R.M., Lintern, M.J., 2010b, April. The new Maia detector system: methods for high definition trace element imaging of natural material. In: AIP Conference Proceedings 1221(1). pp. 9–17.
Ryan, C., Siddons, D., Kirkham, R., Li, Z., De Jonge, M., Paterson, D., Cleverley, J., Kuczewski, A., Dunn, P., Jensen, M., De Geronimo, G., 2013. The Maia detector array and X-ray fluorescence imaging system: locating rare precious metal phases in complex samples. In: Proceedings of SPIE-The International Society for Optical Engineering. Vol. 8851. SPIE.
Ryan, C.G., Siddons, D.P., Kirkham, R., Li, Z.Y., de Jonge, M.D., Paterson, D.J., Kuczewski, A., Howard, D.L., Dunn, P.A., Falkenberg, G., Boesenberg, U., 2014. Maia X-ray fluorescence imaging: capturing detail in complex natural samples. J. Phys.: Conf. Ser. 499 (1), 012002 IOP Publishing.
Ryan, C., Kirkham, R., Parry, D., Moorhead, G., Jensen, M., Hogan, S., Faulks, A., Dunn, P., Dodanwela, R., Fisher, L., Pearce, M., 2018a. Maia Mapper: high Definition XRF Imaging of Geological Samples at Intermediate Spatial Scales. Microsc. Microanal. 24 (S2), 110–111.
Ryan, C.G., Kirkham, R., Moorhead, G.F., Parry, D., Jensen, M., Faulks, A., Hogan, S., Dunn, P.A., Dodanwela, R., Fisher, L.A., Pearce, M., 2018b. Maia Mapper: high definition XRF imaging in the lab. J. Instrum. 13 (03), C03020.
Schumann, D., Fuchs, S., Stromberg, J., Laquerre, A., Mayer, D., Phaneuf, M.W., Vali, H., Banerjee, N., 2014. Combining Terapixel-Scale SEM Imaging and High-Resolution TEM Studies for Mineral Exploration. Microsc. Microanal. 20 (S3), 1008–1009.
Shuster, J., Johnston, C.W., Magarvey, N.A., Gordon, R.A., Barron, K., Banerjee, N.R., Southam, G., 2015. Structural and Chemical Characterization of Placer Gold Grains: implications for Bacterial Contributions to Grain Formation. Geomicrobiol J. 32, 158–169.
Simon, G., Huang, H., Penner-Hahn, J.E., Kesler, S.E., Kao, L.S., 1999. Oxidation state of gold and arsenic in gold-bearing arsenian pyrite. Am. Mineral. 84 (7–8), 1071–1079.
Sutton, S.R., Bertsch, P.M., Newville, M., Rivers, M., Lanzirotti, A., Eng, P., 2002. Microfluorescence and microtomography analyses of heterogeneous earth and environmental materials. Rev. Mineral. Geochem. 49 (1), 429–483.
Sykora, S., Cooke, D.R., Meffre, S., Stephanov, A.S., Gardner, K., Scott, R., Selley, D., Harris, A.C., 2018. Evolution of Pyrite Trace Element Compositions from Porphyry-Style and Epithermal Conditions at the Lihir Gold Deposit: implications for Ore Genesis and Mineral Processing. Econ. Geol. 113, 193–208.
Tardani, D., Reich, M., Deditius, A.P., Chryssoulis, S., Sánchez-Alfaro, P., Wrage, J., Roberts, M.P., 2017. Copper–arsenic decoupling in an active geothermal system: a link between pyrite and fluid composition. Geochim. Cosmochim. Acta 204, 179–204.
Walker, S.R., Jamieson, H.E., Lanzirotti, A., Andrade, C.F., Hall, G.E., 2005. The speciation of arsenic in iron oxides in mine wastes from the Giant gold mine, NWT: application of synchrotron micro-XRD and micro-XANES at the grain scale. Can. Mineral. 43 (4), 1205–1224.
Wang, P., Liu, Y., Menzies, N.W., Wehr, J.B., de Jonge, M.D., Howard, D.L., Kopittke, P.M., Huang, L., 2016. Ferric minerals and organic matter change arsenic speciation in copper mine tailings. Environ. Pollut. 218, 835–843.